Geophysical Journal International

Geophys. J. Int. (2015) **202,** 446–453 doi: 10.1093/gji/ggv157

GJI Mineral physics, rheology, heat flow and volcanology

The collapse of Bárðarbunga caldera, Iceland

B. Riel,[1] P. Milillo,[1,2] M. Simons,[1] P. Lundgren,[3] H. Kanamori[1] and S. Samsonov[4]

[1]*Seismological Laboratory, California Institute of Technology,* 1200 *E. California Blvd., Pasadena, CA* 91125, *USA. E-mail: briel@caltech.edu*
[2]*Scuola di Ingegneria, Università degli Studi della Basilicata, Viale dell'Ateneo Lucano* 10, *I*-85100 *Potenza, Italy*
[3]*Jet Propulsion Laboratory,* 4800 *Oak Grove Dr., Pasadena, CA* 91109, *USA*
[4]*Canada Centre for Mapping and Earth Observation, Natural Resources, Ottawa, ON K*1*S* 5*K*2, *Canada*

Accepted 2015 April 8. Received 2015 April 2; in original form 2015 January 21

SUMMARY

Lying below Vatnajökull ice cap in Iceland, Bárðarbunga stratovolcano began experiencing wholesale caldera collapse in 2014 August 16, one of the largest such events recorded in the modern instrumental era. Simultaneous with this collapse is the initiation of a plate boundary rifting episode north of the caldera. Observations using the international constellation of radar satellites indicate rapid 50 cm d^{-1} subsidence of the glacier surface overlying the collapsing caldera and metre-scale crustal deformation in the active rift zone. Anomalous earthquakes around the rim of the caldera with highly nondouble-couple focal mechanisms provide a mechanical link to the dynamics of the collapsing magma chamber. A model of the collapse consistent with available geodetic and seismic observations suggests that the majority of the observed subsidence occurs aseismically via a deflating sill-like magma chamber.

Key words: Satellite geodesy; Radar interferometry; Magma chamber processes; Calderas; Remote sensing of volcanoes.

1 INTRODUCTION

In 2014 August 16, a swarm of earthquakes was detected underneath Bárðarbunga caldera in Iceland, a stratovolcano located within the Eastern Volcanic Zone (EVZ) and completely covered by the Vatnajökull ice cap (NEIC 2014). These earthquakes signaled the onset of subsurface magma movement. As magma propagated out of the confines of the caldera, earthquake activity tracked its motions, revealing the emplacement of a large dyke along a northeast oriented fissure swarm of the Bárðarbunga volcanic system, consistent with a plate boundary rifting event (Gudmundsson *et al.* 2014; Sigmundsson *et al.* 2014). The dyke intrusion triggered an effusive eruption 40 km away from the caldera at the surface of the Holuhraun lava field north of Vatnajökull beginning in 2014 August 29. Prior to the surface eruption, geodetic observations revealed that the ice over the caldera was subsiding rapidly, with measured rates of approximately 50 cm d^{-1} (Fig. 1). The rapid subsidence was accompanied by moderate earthquakes ($M_w > 5$) with epicentres concentrated along the caldera rim (Fig. 2). Nearly all of these earthquakes exhibited anomalous behaviour with large deviations from traditional double-couple sources (i.e. motion confined to a shear fault plane; Aki & Richards 2002). These earthquakes appear to be the manifestations of simultaneous vertical compression and outward horizontal expansion. Such motion is commonly interpreted as a compensated linear vector dipole (CLVD; Knopoff & Randall 1970). The close spatiotemporal association of the caldera collapse, anomalous seismicity and large-scale rifting provides a unique opportunity to study the mechanics of a caldera collapse in a basaltic system. The large subsidence within the caldera rim, which has never been previously observed at Bárðarbunga, provides critical constraints on the collapse sequence within the caldera.

Since the start of the eruption, a suite of synthetic aperture radar (SAR) images over northwest Vatnajökull and adjacent regions has been acquired by the international constellation of radar satellites. With these images, we can use interferometric SAR (InSAR) to measure surface deformation between two successive SAR images along a line-of-sight (LOS) direction (e.g. Simons & Rosen 2007). We use images acquired by the COSMO-SkyMed (CSK) constellation, which consists of four X-band radar satellites operated by the Italian Space Agency (ASI), to image ground deformation within the vicinity of the Bárðarbunga caldera (Fig. 1). One-day separation between CSK images over the collapsing ice-covered caldera permits the formation of high-resolution interferograms with good coherence, providing snapshots of daily subsidence of the overlying ice. We complement the CSK data with 24- and 48-d-interval InSAR observations from RADARSAT-2 (RS2), a C-band satellite operated by the Canadian Space Agency, to measure ground deformation in ice-free regions north of Vatnajökull. This deformation primarily results from emplacement of an intrusive dyke, producing 1.5 m of surface ground motion very close to the dyke and measurable deformation as far as 60 km away from the surface trace. Near Herðubreið volcano northeast of Askja, a cluster of earthquakes is associated with left-lateral fault motion where discrete centimetre-scale surface rupture can be observed. The left-lateral motion agrees with the previously inferred bookshelf faulting for that area and implies that dyke emplacement enhanced the background stress field in the

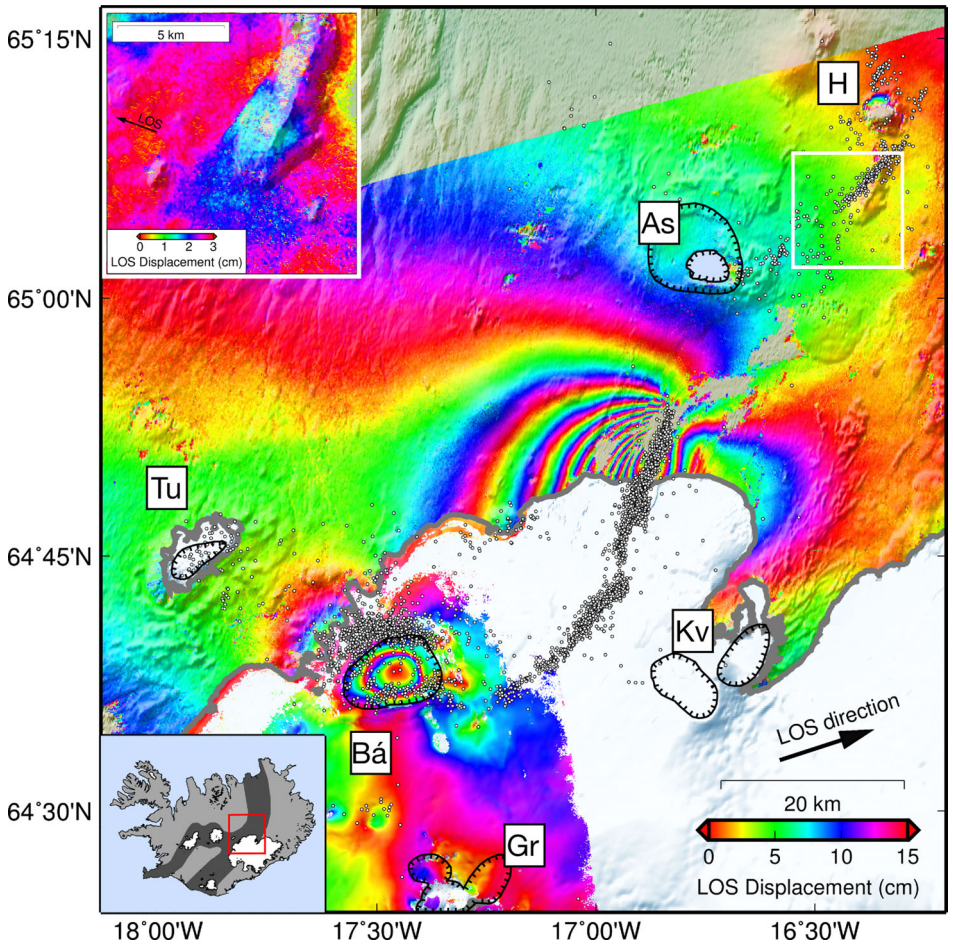

Figure 1. Map of northwestern Vatnajökull, Iceland with the locations of known calderas/volcanos indicated by barbed lines: As, Askja; Bá, Bárðarbunga; Gr, Grímsvötn, H, Herðubreið; Kv, Kverkfjöll; Tu, Tungnafellsjökull. Coloured fringes represent contours of the line-of-sight (LOS) component of ground motion at 15 cm per colour cycle. Areas of high interferometric phase noise have been masked out. The interferogram over the ice was formed from COSMO-SkyMED (CSK) images acquired from 2014 September 12–13 while the 24-d interval interferogram over the ground was formed from RADARSAT-2 (RS2) images acquired on 2014 August 8 and September 1. A clear bullseye pattern over the Bárðarbunga caldera indicates subsidence of the glacier surface. The RS2 interferogram shows the effects of the rifting associated with spreading of the ground away from the active dyke. Black arrow indicates the satellite-to-ground direction for both the CSK and RS2 interferograms. White dots indicate earthquakes that occurred between 2014 August 15 and 2015 February 1, as recorded by the SIL network in Iceland (Böðvarsson *et al.* 1999). Lower left inset shows the location of the study area in Iceland with respect to the glaciers and active volcanic zones (dark grey shading). Upper left inset shows surface rupture near the Herðubreið volcano (denoted by white box) observed in the RS2 interferogram.

Askja rift segment (Green *et al.* 2014; Gudmundsson *et al.* 2014). In the ice-free areas adjacent to and west of Bárðarbunga caldera, inspection of the LOS displacements in the RS2 data reveals several centimetres of motion consistent with a deflating magma chamber beneath the caldera.

2 GEODETIC AND SEISMIC DATA

We formed five 1-d interferograms from CSK images acquired on August 27–28, September 12–13, September 13–14, September 17–18 and October 19–20 (Fig. 2). All interferograms show strong subsidence signals within the caldera boundary, presumably due to subsidence of the caldera floor. While melting of the overlying ice at its base could also result in the observed subsidence, there has been no evidence of anomalous glacial outwash or changes in the ice flow rates for the central Bárðarbunga caldera (Sigmundsson *et al.* 2014). The first two and the last interferogram show similar, axisymmetric bullseye patterns due to the subsidence of the ice over the caldera. However, only a day after the September 12–13 interferogram, the September 13–14 interferogram shows a distinctly different deformation pattern with greater displacement near the northern rim of the caldera. Because ground displacement in one satellite line-of-sight direction is generally a combination of horizontal and vertical motion, we use the method of Yun *et al.* (2006) to estimate the ratio of horizontal to vertical motion on the ice by comparing interferograms with different viewing geometries (Supporting Information Fig. S1). We estimate that the ratio of horizontal to vertical motion does not exceed ≈0.3 within the caldera, and any horizontal motion is diminished close to the centre of the subsidence signal. Thus, assuming purely vertical motion, we can extract profiles across the caldera to estimate instantaneous subsidence rate for each of the interferograms (Supporting Information Fig. S2). The northward trending subsidence pattern in the September 13–14 interferogram is clearly associated with a sharp increase in apparent instantaneous subsidence rate over the background rate: 20 cm increase in the centre of the caldera and 25 cm on the northern edge of the caldera.

Two earthquakes with M_w 4.9 and M_w 5.3 occurred on the north rim of the caldera during the time spans of the September 13–14

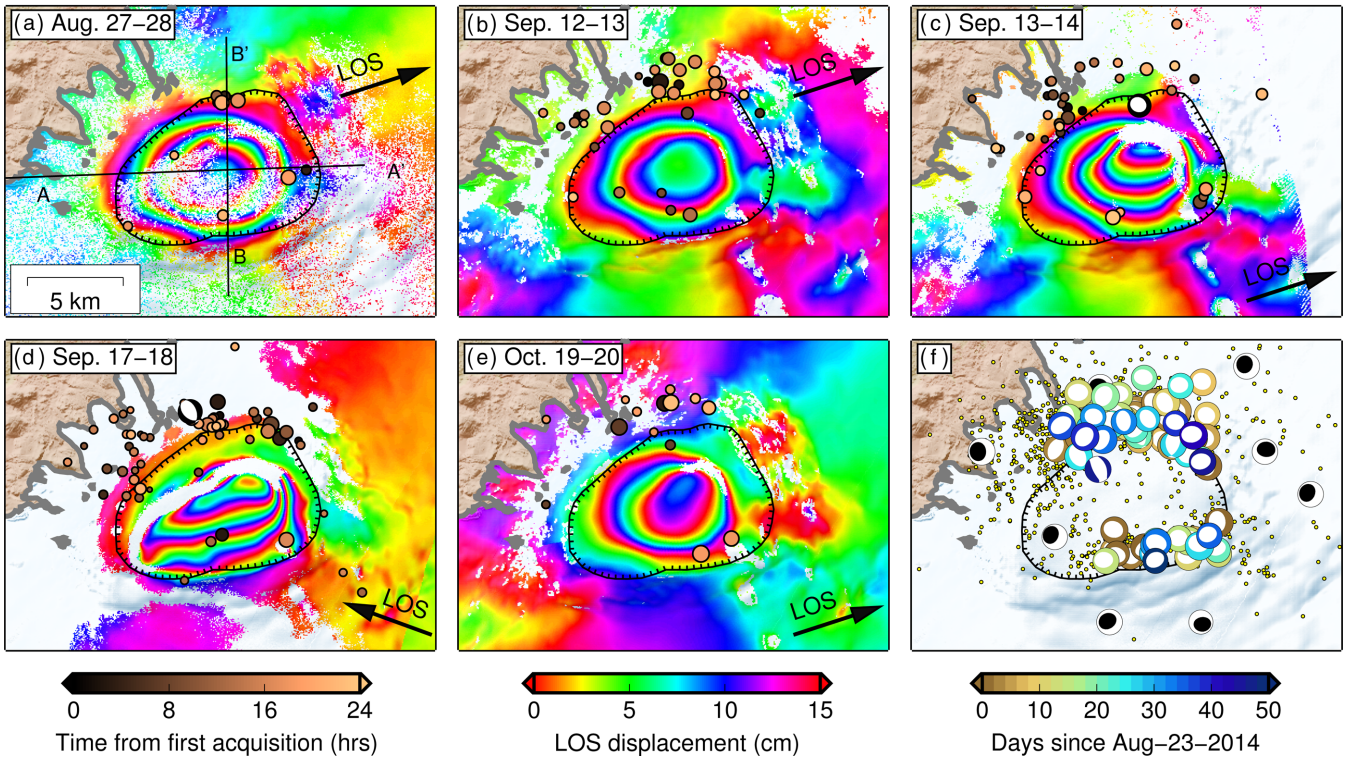

Figure 2. (a)–(e) Evolution of subsidence within the caldera observed from five 1-d interval CSK interferograms. Note the similarity in LOS directions for the interferograms, with the exception of the September 17–18 interferogram. Coloured circles indicate earthquakes that occurred during the time span of the interferogram and are coloured by hours elapsed from the acquisition time of the first image of a given pair. Earthquakes with $M_w > 4.9$ are shown with focal mechanisms derived from moment tensors obtained from the GFZ Potsdam catalog (Centre 1993). The location of the transects in Supporting Information Fig. S2 are indicated in the first panel for the August 27–28 interferogram. (f) Distribution of all seismicity near the caldera between 2014 August 16 to October 21. The coloured focal mechanisms are coloured by days elapsed since 2014 August 23. Yellow dots denote the locations of the earthquakes presented in Fig. 1. The black focal mechanisms with vertical tensional axes correspond to selected CLVD events at Bárðarbunga between 1976 and 1996 (Nettles & Ekström 1998).

and September 17–18 interferograms, respectively (Fig. 2). These two earthquakes were part of a persistent sequence of $M_w > 5$ earthquakes along the rim of the caldera with highly nondouble-couple characteristics, exhibiting dominant vertical compressional axes and horizontal expansions consistent with CLVDs (Fig. 2) (Centre 1993). The focal mechanisms for this sequence of events are consistent between different earthquake catalogs (Supporting Information Table S1). While previous studies of global CLVD earthquakes in the vicinity of active volcanoes have shown that such earthquakes tend to have longer-than-average source durations for their magnitudes, estimates of the magnitudes themselves are weakly dependent on the complexity of the source time functions (Shuler *et al.* 2013a,b). Therefore, the small differences in moment magnitudes between different catalogues for the current event (Supporting Information Table S1) suggests that the magnitudes are correct to within approximately 0.1 magnitude unit.

The M_w 4.9 event has a clear CLVD component in the moment tensor while the M_w 5.3 event appears to show more normal fault motion. The location, size and focal mechanisms of these events, and the absence of similar events during the time spans of the August 27–28, September 12–13 and October 19–20 interferograms, suggests that the asymmetry of the September 13–14 and September 17–18 interferograms is linked to the occurrence of the larger earthquakes on the northern rim. A simple relationship between earthquake size and ground displacement, such as assuming seismic potency is proportional to a really integrated displacements of the ice surface, does not appear to apply to these events since the potency associated with the earthquake that occurred during the September 13–14 interval was nearly five times less than the earthquake that occurred during the September 17–18 interval, yet the estimated volume change within the caldera as estimated from the integrated displacements is larger for the former (Fig. 3d). Therefore, most of the subsidence occurs aseismically while the larger $M_w > 5$ events may produce localized additional displacements of up to 25 cm along the caldera rim as measured at the ice surface.

3 SOURCE MODELS FOR RIFT ZONE AND MAGMA CHAMBER

Experimental and numerical studies of caldera collapse consistently show that the size, shape and depth of subsurface magma chambers strongly affect the final geometry of the collapsed caldera, as well as the rate at which it will form Roche *et al.* (2000), Geyer *et al.* (2006), Gudmundsson (2007, 2008). In order to estimate the depth of a subsurface magma chamber while avoiding modelling errors due to uncertain ice-rock coupling, we consider LOS displacements of the subsidence signal from the ice-free areas in interferograms formed from longer time interval RS2 images (24 and 48 d, Supporting Information Fig. S8). We also include data from continuous global positioning system (GPS) stations located north of Vatnajökull (Sigmundsson *et al.* 2014). As part of the analysis, we remove ground displacements due to the rift zone by estimating an elastic model for tensile opening along the dyke interface using a collection of RS2 and CSK interferograms and the GPS data (see Supporting

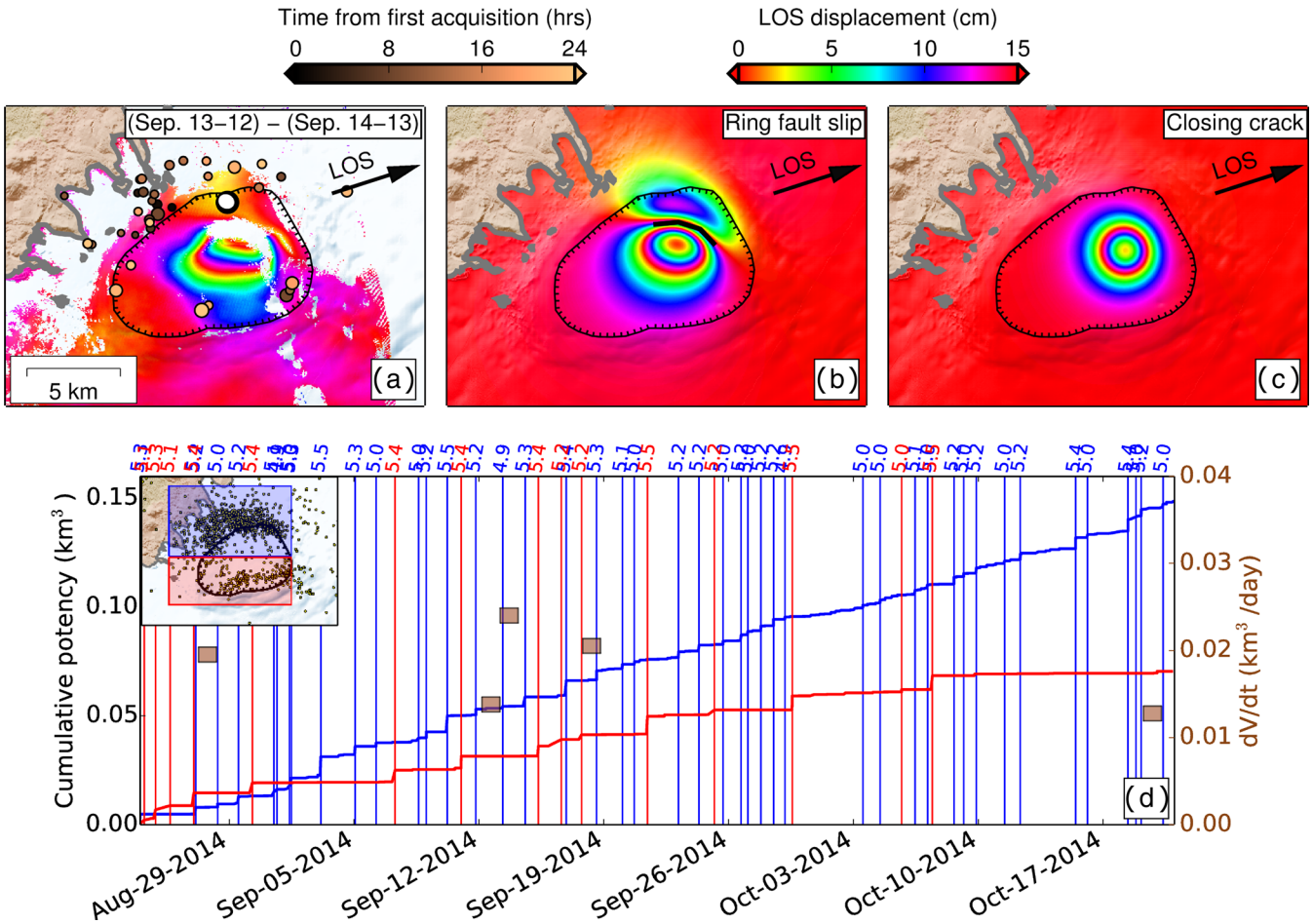

Figure 3. (a) Difference between September 12–13 and September 13–14 interferograms for isolating the ground deformation associated with a M_w 4.9 earthquake that occurred on September 14. Also shown are synthetic LOS displacements due to slip along a vertical ring fault (b) and a closing crack (c). For the ring fault (thick black line), the fault is placed at a depth of 2 km with a width of 1 km and approximately 3 m of normal motion. The closing crack is simulated using the model of Fialko *et al.* (2001) at a depth of 2 km, a radius of 1 km and a volume change of 0.003 km^3. (d) Seismic potency for the northern and southern halves of the caldera compared with estimated volume change rate (dV/dt) within the caldera inferred from the 1-d interferograms. The thick blue and red lines correspond to the cumulative potency of the northern and southern regions, respectively, of the caldera. To calculate seismic potency, we divide the seismic moment by a shear modulus of 24 GPa. Thin vertical lines mark the occurrence of earthquakes greater than M_w 4.9. The shaded brown boxes show the time spans of each 1-d interferogram and the estimated volume change during that time span (right ordinate). The volume change for each interferogram was computed by integrating the projected vertical displacements within the caldera boundary.

Information Section S1.1; Fig. S4). While the geodetic data alone cannot resolve opening of the dyke under the ice, the robust components of the model include approximately 5 m of opening in the upper 5 km of the resolvable dyke segment (equivalent to 200–300 yr of cumulative plate motion) and peak geodetic potency occurring at a shallower depth (≈2 km) than the peak earthquake density, which occurs at around 6 km depth (Sigmundsson *et al.* 2014; Supporting Information Fig. S6). These results agree with estimates of the dyke geometry from other studies (e.g. Gudmundsson *et al.* 2014; Sigmundsson *et al.* 2014).

After removal of the rift zone signal, we model the chamber as a collapsing horizontal circular crack in an elastic half-space (Fialko *et al.* 2001; Supporting Information Section S1.2). The parameterization of the chamber parameters is such that there are strong trade-offs between the chamber depth, radius and excess pressure (difference between the magma chamber and lithostatic pressures). However, we are able to resolve a consistent depth-to-radius ratio of approximately 3.6 (Supporting Information Fig. S7). By adjusting the excess pressure, we can explain the geodetic observations equally well with a shallow, small chamber or a deep, larger chamber. Therefore, determining the 'true' depth of the magma chamber would require other independent observations, that is re-located seismicity of earthquakes occurring within and around the caldera or an upper bound on the allowable values for excess pressure. Nevertheless, the ability of our model to fit the displacements at distances greater than three times the chamber radius validates the assumption of a symmetric source with a uniform pressure difference since no obvious asymmetries appear in the residuals. Steady deflation of the chamber is thus the primary contributor to subsidence observations both on and off the ice. While we cannot rule out the possibility of additional deeper magma chambers (depth >10 km), our lack of reliable ground measurements over the caldera limits our ability to resolve multiple chambers.

4 DISCUSSION

One of the most interesting aspects of the collapse sequence has been the occurrence of the moderate earthquakes along the caldera rim with large CLVD components in their focal mechanisms. Assuming that the background subsidence rate is nearly constant

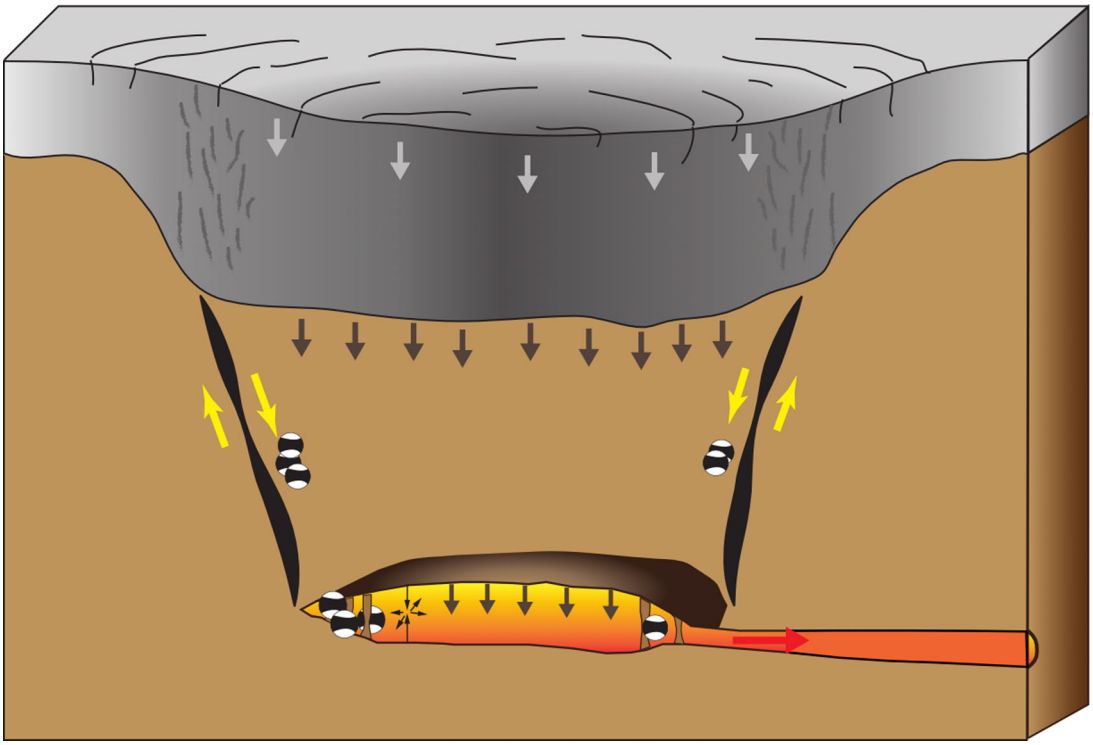

Figure 4. A conceptual model for the mechanics of the collapsing caldera. Magma migration out of the chamber into the dyke system causes depressurization of the chamber. The deflating chamber results in subsidence of a coherent block above the chamber, as well as subsidence of the overlying ice. Sustained depressurization of the chamber leads to failure of internal support structures (causing seismic events marked by inward vertical motion and outward horizontal expansion) or rupturing of curved, inward-dipping ring faults. Cross-sections of focal mechanisms representative of these events are shown on the edge of the chamber.

between September 12–14, we can isolate the ground deformation associated with one of the earthquakes (M_w 4.9 on September 13) by forming a residual interferogram of the difference between the September 12–13 and September 13–14 CSK interferograms since only the September 13-14 image spanned the time of the earthquake (Fig. 3a). The highly localized deformation due to the earthquake indicates that the source is most likely shallow. For earthquakes with vertical CLVD focal mechanisms in the vicinity of volcanoes, the two most likely physical processes are rupture on curved ring faults or opening/closing of a crack under tension/compression (Acocella 2007; Shuler *et al.* 2013b). Static simulations for both processes require source depths of approximately 2 km to roughly match the InSAR observations (Figs 3b and c). For reference, a M_w 4.9 event with an effective shear modulus of 5 GPa (typical for shallow depths in volcanic systems within an extensional regime (Smith *et al.* 1996)) has a seismic potency of approximately 0.004 km^3. However, the simulated ring fault rupture requires a much larger potency (≈0.01 km^3), which implies a very low effective shear modulus (≈1 GPa) consistent with very weak materials such as water-saturated basaltic tuff. While the closing crack provides a more realistic measure of potency (equivalent volume change of about 0.003 km^3), the synthetic ground deformation lacks the asymmetry observed in the residual interferogram. Therefore, for both cases, it is likely that the ground deformation is a combination of seismic deformation (due to ring faulting or a closing crack) and aseismic slip on the ring fault. The inconsistency between earthquake size and ground deformation (Fig. 3d) suggests that the amount of aseismic slip per event is highly variable.

Based on the seismic evidence and the inversion results for the chamber geometry, we propose a model for the sequence of the caldera collapse and dyke emplacement (Fig. 4). The initial seismic activity on the southern edge of the caldera and subsequent propagation of an oblique dyke caused depressurization of a magma chamber that can be approximated as a horizontal circular sill. Magma migrated out of the chamber to the short, oblique dyke and eventually migrated to the larger, regional-scale dyke. The underpressure in the magma chamber resulted in subsidence of the caldera surface and overlying ice. Stress concentrations in the vicinity of the deflating magma chamber led to the initiation of $M_w > 5$ seismic events located along the caldera rim. The large CLVD components in the earthquake focal mechanisms indicate a seismic process characterized either by downward vertical motions and horizontal expansions or rupture on a curved fault. The former process has been observed in mine collapses where rapid closing of a horizontally oriented underground cavity (the mine) leads to CLVD components in the seismic moment tensor (Dreger *et al.* 2008). A mine collapse mechanism could imply failure of brittle support structures within the partially molten magma chamber due to large compressive stresses, which would require a larger (and thus deeper) magma chamber since the earthquake clusters on the northern and southern rim of the caldera are separated by approximately 8–10 km. Alternatively, the deflating chamber could impart large shear stresses on existing ring faults, leading to seismogenic slip on limited portions of a ring fault. Static stress changes associated with both mechanisms could then trigger larger aseismic slip on the ring fault with slip most likely confined to shallower depths.

Earthquakes with significant nondouble-couple components in their focal mechanisms have occurred at Bárðarbunga in the decades prior to the current event (Supporting Information Table S2; Nettles & Ekström 1998; Konstantinou *et al.* 2003; Tkalčić *et al.* 2009). However, the polarities of the focal mechanisms for the current Bárðarbunga eruption are opposite to those observed for

the earlier earthquakes, that is vertical compressional axes for the former and tensional axes for the latter (Fig. 2f). One interpretation of these earlier events suggested that their faulting mechanisms are primarily due to rupture on outward dipping ring faults which are activated by inflation of a very shallow magma chamber (Nettles & Ekström 1998). However, this interpretation is highly nonunique, since a deflating magma chamber below the ring faults could also produce similar focal mechanisms (Ekström 1994). Our inversion results for the magma chamber predict a chamber radius smaller than the caldera radius for chamber depths less than 15 km (Supporting Information Figs S7 and S8), which implies inward dipping ring faults. The dip of the ring faults controls the rupture arc-length necessary to create the CLVD focal mechanisms. For this geometry, the earlier events can be explained by inflation of the magma chamber, leading to reverse motion on those ring faults.

In addition to mine collapses and ring fault rupture, earthquakes with large CLVD components like the ones observed on the rim of the Bárðarbunga caldera have been observed for tensile failure due to high fluid pressure (Sipkin 1986) and magma injection in water-saturated environments (Kanamori *et al.* 1993). An earthquake with a strong CLVD component was observed near Tori Shima, Japan in 1984. Since the earthquake was tsunamigenic, the preferred explanation was horizontal injection of magma into water-saturated sediment with a volumetric component resulting from the explosive magma-water interaction (Kanamori *et al.* 1993). A global search for earthquakes prior to 2013 with vertical-CLVD mechanisms revealed ≈100 vertical-CLVD earthquakes located near active volcanoes over the past century (Shuler *et al.* 2013a). Thus, the close temporal and spatial association of the current Bárðarbunga anomalous events with the active fissuring lends credibility to a collapse mechanism driven by a drop in magma pressure. A sudden vertical collapse with no volume change would be characterized by downward vertical and outward horizontal motions.

Our model of caldera collapse due to magma withdrawal has been proposed for volcanic systems in Iceland neighbouring Bárðarbunga. North of the EVZ is the Northern Volcanic Zone (NVZ), consisting of five *en echelon* volcanic systems aligned with the boundary of the North American and European plates (Einarsson 1991). Within the NVZ, the Krafla caldera system was the site of a major rifting event between 1975 and 1984. Eruptive activity initiated with inflation of the central caldera, which then underwent rapid deflation, leading to lateral basaltic magma injection into a northward trending fissure swarm. A shallow magma chamber at approximately 3 km depth has been inferred at Krafla via inversions of geodetic observations (Ewart *et al.* 1991). Seismic tremor amplitude associated with dyke emplacement was correlated with subsidence at the caldera (Einarsson 1991), suggesting a mechanistic link between chamber pressure and stress on the dyke. Numerical models support the hypothesis that magma pressure, dyke overpressure, and background tectonic stresses are the primary factors controlling dyke propagation (Buck *et al.* 2006). Recent studies of the current dyke emplacement at Bárðarbunga also predict a feedback mechanism where dyke-induced stresses trigger seismicity at the caldera itself (Gudmundsson *et al.* 2014). Kinematically, however, the two volcanic systems are quite different since the maximum subsidence for Krafla (2 m) was substantially smaller than that of Bárðarbunga (about 60 m). Additionally, the Krafla episode experienced periodic inflation/deflation over 10 yr whereas Bárðarbunga has thus far only experienced rapid deflation and over a much shorter time period.

On a global scale, there have only been a few observed eruptive events and subsequent caldera collapses in basaltic systems, although none with volume changes as large as Bárðarbunga. The 1968 caldera collapse at Isla Fernandina in the Galápagos Islands occurred on a single shield volcano, and aerial observations indicated that the caldera floor collapsed 300 m as a 3 km wide coherent block with motion confined to an elliptical boundary fault formed from a prior collapse event (Simkin & Howard 1970; Filson *et al.* 1973; Francis 1974). In 2000, the Miyakejima stratovolcano in the Izu-Bonin volcanic chain experienced 12 d of increased seismicity due to magma intrusion at its northwest flanks, which was then followed by a minor phreatic eruption and formation of a collapsed caldera 1.6 km in diametre (Ukawa *et al.* 2000; Geshi *et al.* 2002). Tiltmeters stationed around the summit indicated intermittent abrupt uplift events superposed on the longer term subsidence. The uplift events were accompanied by very long period (VLP) seismic events detectable over a wide area (Ukawa *et al.* 2000; Kumagai *et al.* 2001). Similar observations were collected for the 2007 Piton de la Fournaise caldera collapse during its largest historical eruption (Michon *et al.* 2009). For Miyakejima, all of the VLP events exhibited large CLVD components for their focal mechanisms, which was explained to be slip on both inward- and outward-dipping faults (Geshi *et al.* 2002; Shuler *et al.* 2013a). 60 km south of the Isla Fernandina caldera, an inflation event occurred at the Sierra Negra caldera which was followed a few years later by a M_w 5.5 CLVD earthquake with a vertical tensional axis (Yun *et al.* 2006; Shuler *et al.* 2013a), consistent with the interpretation of the older Bárðarbunga events being caused by inflation of a central magma chamber.

5 CONCLUSIONS

While the unique geodetic observations of ground deformation within and around the Bárðarbunga caldera during its collapse were the first of its kind for the caldera, there are still large uncertainties regarding the mechanics of the collapse process. The difficulties associated with the unknown interaction between the overlying glacier and the bedrock limits the spatial extent of usable data for estimating the geometry of the underlying magma chamber and active ring fault systems. We have shown that a majority of the ice-free ground deformation can be attributed to steady deflation of a horizontal circular sill. However, the physical process driving the anomalous $M_w > 5$ earthquakes along the caldera rim is still uncertain. The geodetic signature of one of these events, as measured by the differences in successive 1-d interferograms over the ice, suggests a shallow seismic source caused by rupture on a ring fault or a rapidly closing crack. Since the amount of ground deformation expected for either seismic mechanism is significantly less than the observed deformation, we believe that the total ground deformation is caused by a combination of seismic processes and aseismic slip on ring faults. However, if the shear modulus in the vicinity of the caldera were much lower than expected (perhaps due to the presence of water-saturated basaltic tuff), then the predicted deformation for the seismic component would be much larger. In that case, the earthquakes can be explained entirely by rupture on dipping ring faults.

ACKNOWLEDGEMENTS

We thank Egill Hauksson and Hilary Martens for discussions in the early phase of this study. We also thank Agust Gudmundsson, Jürg Schuler and three anonymous reviewers for their helpful comments and for improving the quality of this manuscript. BR was supported under a National Aeronautics and Space Administration (NASA)

Earth and Space Science Fellowship. Part of this research was carried out at the Jet Propulsion Laboratory and the California Institute of Technology under a contract with NASA and funded through the President's and Director's Fund Program. This research was carried out using COSMO-SkyMed (CSK ®) products delivered under an Italian Space Agency (ASI) license and is made possible through a collaboration between JPL/Caltech/CIDOT and NASA/ASI.

REFERENCES

Acocella, V., 2007. *Earth-Sci. Rev.,* **85**(3), 125–160.

Adam, L. & Otheim, T., 2013. *J. geophys. Res.,* **118**(3), 840–851.

Aki, K. & Richards, P.G., 2002. *Quantitative Seismology,* Vol. 1, University Science Books.

Böðvarsson, R., Rögnvaldsson, S.T., Slunga, R. & Kjartansson, E., 1999. The SIL data acquisition system—at present and beyond year 2000, *Phys. Earth planet. Inter.,* **113**(1), 89–101.

Buck, W.R., Einarsson, P. & Brandsdóttir, B., 2006. Tectonic stress and magma chamber size as controls on dike propagation: constraints from the 1975–1984 Krafla rifting episode, *J. geophys. Res.: Solid Earth (1978–2012),* **111,** B12404, doi:10.1029/2005JB003879.

Centre, G.D., 1993. Geofon seismic network. Available at: deutsches geoforschungszentrum gfz.other/seismic network (last accessed 2014 October 13).

Dreger, D.S., Ford, S.R. & Walter, W.R., 2008. Source analysis of the crandall canyon, Utah, mine collapse, *Science,* **321**(5886), 217–217.

Einarsson, P., 1991. Earthquakes and present-day tectonism in Iceland, *Tectonophysics,* **189**(1), 261–279.

Ekström, G., 1994. Anomalous earthquakes on volcano ring-fault structures, *Earth planet. Sci. Lett.,* **128**(3), 707–712.

Ewart, J.A., Voight, B. & Björnsson, A., 1991. Elastic deformation models of krafla volcano, iceland, for the decade 1975 through 1985, *Bull. Volcanol.,* **53**(6), 436–459.

Fialko, Y., Khazan, Y. & Simons, M., 2001. Deformation due to a pressurized horizontal circular crack in an elastic half-space, with applications to volcano geodesy, *Geophys. J. Int.,* **146**(1), 181–190.

Filson, J., Simkin, T. & Leu, L.-k., 1973. Seismicity of a caldera collapse: Galapagos islands 1968, *J. geophys. Res.,* **78**(35), 8591–8622.

Francis, T., 1974. A new interpretation of the 1968 Fernandina caldera collapse and its implications for the mid-oceanic ridges, *Geophys. J. Int.,* **39**(2), 301–318.

Geshi, N., Shimano, T., Chiba, T. & Nakada, S., 2002. Caldera collapse during the 2000 eruption of Miyakejima volcano, Japan, *Bull. Volcanol.,* **64**(1), 55–68.

Geyer, A., Folch, A. & Martí, J., 2006. Relationship between caldera collapse and magma chamber withdrawal: an experimental approach, *J. Volc. Geotherm. Res.,* **157**(4), 375–386.

Green, R.G., White, R.S. & Greenfield, T., 2014. Motion in the north Iceland volcanic rift zone accommodated by bookshelf faulting, *Nat. Geosci.,* **7**(1), 29–33.

Gudmundsson, A., 2007. Conceptual and numerical models of ring-fault formation, *J. Volc. Geotherm. Res.,* **165,** 142–160.

Gudmundsson, A., 2008. Magma-chamber geometry, fluid transport, local stresses and rock behaviour during collapse caldera formation, *Dev. Volcanol.,* **10,** 313–349.

Gudmundsson, A., Lecoeur, N., Mohajeri, N. & Thordarson, T., 2014. Dike emplacement at Bárðarbunga, Iceland, induces unusual stress changes, caldera deformation, and earthquakes, *Bull. Volcanol.,* **76**(10), 1–7.

Kanamori, H., Ekström, G., Dziewonski, A., Barker, J.S. & Sipkin, S.A., 1993. Seismic radiation by magma injection: an anomalous seismic event near Tori Shima, Japan, *J. geophys. Res.: Solid Earth (1978–2012),* **98**(B4), 6511–6522.

Knopoff, L. & Randall, M.J., 1970. The compensated linear-vector dipole: A possible mechanism for deep earthquakes, *J. geophys. Res.,* **75**(26), 4957–4963.

Konstantinou, K., Kao, H., Lin, C.H. & Liang, W.T., 2003. Analysis of broad-band regional waveforms of the 1996 September 29 earthquake at Bárdarbunga volcano, central Iceland: investigation of the magma injection hypothesis, *Geophys. J. Int.,* **154**(1), 134–145.

Kumagai, H., Ohminato, T., Nakano, M., Ooi, M., Kubo, A., Inoue, H. & Oikawa, J., 2001. Very-long-period seismic signals and caldera formation at Miyake Island, Japan, *Science,* **293**(5530), 687–690.

Michon, L., Villeneuve, N., Catry, T. & Merle, O., 2009. How summit calderas collapse on basaltic volcanoes: new insights from the april 2007 caldera collapse of Piton de la Fournaise volcano, *J. Volc. Geotherm. Res.,* **184**(1), 138–151.

National Earthquake Information Center, United States Geological Survey, 2014. Retrieved from http://earthquake.usgs.gov

Nettles, M. & Ekström, G., 1998. Faulting mechanism of anomalous earthquakes near Bardarbunga volcano, Iceland, *J. geophys. Res.: Solid Earth (1978–2012),* **103**(B8), 17 973–17 983.

Roche, O., Druitt, T. & Merle, O., 2000. Experimental study of caldera formation, *J. geophys. Res.: Solid Earth (1978–2012),* **105**(B1), 395–416.

Shuler, A., Nettles, M. & Ekström, G., 2013a. Global observation of vertical-CLVD earthquakes at active volcanoes, *J. geophys. Res.,* **118**(B1), 138–164.

Shuler, A., Ekström, G. & Nettles, M., 2013b. Physical mechanisms for vertical-CLVD earthquakes at active volcanoes, *J. geophys. Res.,* **118**(B4), 1569–1586.

Sigmundsson, F. *et al.*, 2014. Segmented lateral dyke growth in a rifting event at Bárdarbunga volcanic system, Iceland, *Nature,* **517,** 191–195.

Simkin, T. & Howard, K.A., 1970. Caldera collapse in the Galápagos islands, 1968 the largest known collapse since 1912 followed a flank eruption and explosive volcanism within the caldera, *Science,* **169**(3944), 429–437.

Simons, M. & Rosen, P., 2007. Interferometric synthetic aperture radar geodesy, *Treatise on Geophysics,* Elsevier, pp. 391–446.

Sipkin, S.A., 1986. Interpretation of non-double-couple earthquake mechanisms derived from moment tensor inversion, *J. geophys. Res.: Solid Earth (1978–2012),* **91**(B1), 531–547.

Smith, R.P., Jackson, S.M. & Hackett, W.R., 1996. Paleoseismology and seismic hazards evaluations in extensional volcanic terrains, *J. geophys. Res.,* **101**(B3), 6277–6292.

Tkalčić, H., Dreger, D.S., Foulger, G.R. & Julian, B.R., 2009. The puzzle of the 1996 Bárdarbunga, Iceland, earthquake: no volumetric component in the source mechanism, *Bull. seism. Soc. Am.,* **99**(5), 3077–3085.

Ukawa, M., Fujita, E., Yamamoto, E., Okada, Y. & Kikuchi, M., 2000. The 2000 Miyakejima eruption: crustal deformation and earthquakes observed by the NIED Miyakejima observation network, *Earth Planet Space,* **52**(8), xix–xxvi.

Yun, S., Segall, P. & Zebker, H., 2006. Constraints on magma chamber geometry at Sierra Negra volcano, Galápagos islands, based on InSAR observations, *J. Volcanol. Geotherm. Res.,* **150**(1), 232–243.

SUPPORTING INFORMATION

Additional Supporting Information may be found in the online version of this paper:

Figure S1. Ascending and descending one-day CSK interferograms with time spans of Sep. 13–14 and Sep. 17–18, respectively. The two viewing geometries allow for separation of LOS displacements into vertical and horizontal components using the method of Yun *et al.* (2006), assuming that the two interferograms are measuring roughly the same ground deformation. While the two interferograms appear to measure similar levels of ice subsidence, the earthquake perturbations are more pronounced for the Sep. 13–14 interferogram (see Fig. 2). Nevertheless, the ratio of horizontal to vertical displacements does not exceed ≈0.3 within the caldera.

Figure S2. Profiles of projected vertical subsidence observed in the five one-day CSK interferograms. Profile locations are shown in Fig. 2. Vertical displacements were computed by dividing the line-of-sight range changes by the cosine of the incidence angle for

each interferogram. Solid lines are constructed from interferogram data with good coherence while the dashed lines interpolate through areas of low coherence. The gold line shows transects extracted from a 2013 one-day interferogram (Fig. S3), confirming that the current subsidence is directly related to the ongoing magmatic activity.

Figure S3. One day interferogram of Bárðarbunga caldera and surrounding ice-covered regions formed from CSK images acquired on June 26, 2013 and June 27, 2013. No significant subsidence over the caldera is observed, although LOS displacements due to ice flow out of the east side of the caldera are consistent with the 2014 interferograms.

Figure S4. Time spans of interferograms used for estimating the distribution of tensile opening along the dike interface. All interferogram time spans are referenced to Aug. 16, 2014, indicated by the vertical dashed line. The yellow lines correspond to RS2 interferograms while the red lines correspond to CSK interferograms. The orbital directions of the images used for the interferograms are indicated as either ascending (ASC) or descending (DESC). The alternating gray and white columns correspond to the temporal subdomains used in the inversion.

Figure S5. Estimated distribution of opening along the dike interface for the time span corresponding to the RS2 interferogram in Fig. 1. The synthetic interferogram (see Fig. S6) is shown above the fault, and the white dots correspond to earthquakes located along the dike using the SIL network.

Figure S6. Synthetic ground deformation for the elastic model of tensile opening along the dike interface. (A) RS2 interferogram from Fig. 1 and GPS displacements with 90% confidence error ellipses used in inversion. (B) Synthetic ground displacements from the estimated model. The modeled LOS displacements include a bilinear ramp to account for orbital errors and long-wavelength deformation. Ellipses represent 90% confidence posterior uncertainties in the modeled GPS displacements. (C) Residual interferogram and GPS displacements after subtracting the synthetic ground displacements. Larger residuals near the surface trace north of Vatnajökull may indicate potential asymmetries due to dike dip not captured in our vertical dike model. (D) Cumulative geodetic potency from the dike model in Fig. S5 for Aug. 16–Sep. 20 vs. a histogram of the depth distribution of earthquakes located along the dike.

Figure S7. (A) Samples for magma chamber depth and radius obtained from an adaptive Metropolis algorithm. Red and blue circles correspond to samples where the prior distribution for the chamber depth has a maximum at 3 and 6 km, respectively. The black dashed lines indicate lines of constant depth-to-radius ratio, h. (B) Samples for magma chamber pressure (in units of the shear modulus μ) and radius.

Figure S8. Modelling of the source magma chamber using geodetic measurements on ice-free areas. The chamber is modeled as a horizontal circular sill at depth. (A) Unwrapped RS2 interferogram formed from images acquired in an ascending orbit on Aug. 1, 2014 and Sep. 18, 2014, and GPS displacements with 90% confidence error ellipses for VONC and HNIF after removing the estimated signal from the rift zone; (B) unwrapped RS2 interferogram from images acquired in a descending orbit on Aug. 27, 2014 and Sep. 20, 2014; (C) modelled GPS displacements and LOS displacements for the ascending interferogram for a chamber at a depth of 8 km and a radius of 2.3 km (location and size indicated by red dashed circle) or a depth of 4 km and radius of 1.1 km (blue dashed circle); (D) modelled LOS displacements for the descending interferogram; (E) residual between (A) and (C); and (F) residual between (B) and (D). The estimated volume changes were 0.43 km^3 and 0.14 km^3 for the ascending and descending interferograms, respectively.

Figure S9. Seismicity rates for earthquakes occurring within the dike (top) and caldera (bottom). The number of earthquakes are binned in latitude and time where 1-day intervals are used for the time bins. The count is saturated at 15 earthquakes/day for visualization clarity. Bins with less than two earthquakes are coloured white. High seismicity rates within the dike for the first 10 days are associated with the initial dike emplacement. While seismicity along the dike has decreased with time, seismicity along the northern rim of the caldera has increased.

Table S1. Comparison of select earthquakes from the GFZ Potsdam and Global CMT (GCMT; Dziewonski *et al.* 1981; Ekström *et al.* 2012) catalogs. Focal mechanisms and moment magnitudes are shown for the earthquakes from each catalog. We compute seismic moment as $M_0 = 1/\sqrt{2}\left(\Sigma_{ij} M_{ij}\right)^{1/2}$. Both the mechanisms and moment magnitudes are consistent between the catalogs.

Table S2. Focal mechanisms and moment magnitudes for CLVD events occurring near Bárðarbunga from 1976–1996. The focal mechanisms were formed using the moment tensor elements estimated by Nettles & Ekström (1998). These prior events exhibit opposite polarities from the current events (vertical tensional vs. compressional axes). (http://gji.oxfordjournals.org/lookup/suppl/doi:10.1093/gji/ggv157/-/DC1)